MATERIALS SCIENCE

Integrating structurally defined DNA-carbon nanotube sensors with machine learning for cancer detection

Piaoyi Chen[1]†, Xin Zheng[2]†, Yinong Li[1], Jian Li[1], Xuan Zhou[1], Yawei Wen[1], Jialong Liu[1], Pengbo Wang[1], Xiaohui Li[2], Runzhe Chen[3], Zhiwei Lin[1,4]*

Liquid biopsy is a promising, noninvasive approach for cancer detection, but current methods often trade off accuracy, operability, and cost. To address these limitations, we introduce an artificial perception system (APS) for liquid biopsy that combines a structurally defined DNA-carbon nanotube sensor array with machine learning (ML) models. The array produces multichannel fluorescence fingerprints from serum, which are decoded by ML models to classify disease state. In a total of 253 serum samples spanning liver, lung, and ovarian cancers and noncancer controls, the APS achieved mean sensitivity of 89% and specificity of 96%. Notably, early-stage lung cancer was detected with 92% sensitivity and 95% specificity at an estimated cost of ~$4 USD per test. Insights from SHAP analysis and Mantel test revealed the detection mechanisms of APS, supporting biological plausibility and clinical translation. These results highlight a path toward accurate, scalable, and affordable multicancer detection and early cancer screening.

INTRODUCTION

Liquid biopsy represents a promising, noninvasive methodology for cancer detection, aiming to read disease states directly from accessible biofluids (*1*–*3*). Existing approaches include targeted molecular assays [e.g., circulating tumor DNA (ctDNA) panels] and untargeted "profile" assays (e.g., high-dimensional proteomics/metabolomics) (*4*–*6*). A third, complementary paradigm, perception-based sensing, seeks to classify complex biochemical mixtures by their holistic fingerprint rather than by resolving or quantifying individual constituents (*7*–*9*). A recent success in this area uses single-wall carbon nanotubes (CNTs) coated with single-stranded DNA (*10*–*13*) or other polymers (*14*–*16*) to create a chemically rich corona that mediates selective interactions with proteins (*17*, *18*), lipids (*19*, *20*), metabolites (*21*–*24*), ions (*25*, *26*), virus (*27*), and disease-relevant molecules (*28*, *29*). Notably, Heller and colleagues established the machine perception liquid biopsy (MPLB) paradigm, achieving high-performance detection of ovarian cancer (OC) (*29*) and intracranial tumors (*30*) using DNA-coated and sp^3 defect-modified CNTs.

Despite these successes, a fundamental strategic challenge persists: Current perception-based sensors often rely on chirality-mixed CNTs or stochastic DNA functionalization. These approaches introduce a degree of structural heterogeneity such as batch-dependent variations in defect density or DNA/polymer conformation, which can obfuscate cross-batch normalization and limit the "learning transfer" required for broader clinical adoption. In contrast, biological olfaction relies on receptors that are genetically encoded and folded into precise, deterministic structures (Fig. 1A). This structural rigor allows the brain to decode stable, reusable representations of complex odors across diverse environments (*31*, *32*).

In this context, we here report an artificial perception system (APS) founded on structure-defined, defect-free DNA-CNT arrays. Unlike previous work that used stochastic sensor engineering, the APS leverages enantiomerically pure, single-chirality CNTs (scCNTs) wrapped with well-defined DNA motifs that we recently established (*33*). These DNA-scCNT hybrids provide not only subnanometer structural uniformity but also deterministic optical footprints, ensuring that every sensor channel yields a reproducible response profile (*34*). By mimicking the combinatorial logic of olfactory perception, the APS transforms subtle serum perturbations into high-dimensional, cohort-specific fingerprints (Fig. 1B).

Our results demonstrate that this structurally-defined array, coupled with ensemble machine learning (ML), achieves the simultaneous discrimination of liver cancer (LC), lung cancer (LuC), and OCs from noncancer (NC) samples with an average accuracy of 88.9% in an external validation cohort. Crucially, when applied to the formidable task of early-stage cancer screening, the APS achieved a sensitivity of 92% and a specificity of 95%, with a projected cost of only ~$4 USD per test. These findings highlight the substantial clinical potential of the APS for noninvasive, cost-effective cancer detection and early screening. By transitioning from structural heterogeneity to defined molecular precision, this work may establish a unified diagnostic framework. This reproducible sensor array mimics biological perception to continuously learn and interpret the complex molecular signatures of the serum multiome, providing a versatile interface for emerging clinical applications.

RESULTS

Construction of multiplexed DNA-scCNT sensor array

We constructed a multiplexed DNA-scCNTs sensor array using six structurally defined single-chirality species, including $(GGC)_2(GC)_3$-(−)(6,4), TTA$(TAT)_2$ATT-(−)(6,5), $C_2(GCCCC)_2$-(+)(7,3), C_3GC_6-GC_4-(−)(7,5), $T_3C_3T_3C_6$-(−)(8,3), and $C_3(CCG)_3$-(+)(9,1). Each nanotube with a defined helicity and handedness is wrapped with its

[1]South China Advanced Institute for Soft Matter Science and Technology, State Key Laboratory of Luminescent Materials and Devices, School of Emergent Soft Matter, South China University of Technology, Guangzhou 510640, China. [2]Department of Clinical Laboratory Medicine, Sun Yat-Sen University Cancer Center, State Key Laboratory of Oncology in South China, Collaborative Innovation Center for Cancer Medicine, Guangzhou 510060, China. [3]Department of Radiation Oncology, Sun Yat-Sen University Cancer Center, State Key Laboratory of Oncology in South China, Collaborative Innovation Center for Cancer Medicine, Guangzhou 510060, China. [4]Guangdong Provincial Key Laboratory of Functional and Intelligent Hybrid Materials and Devices, Guangdong Basic Research Center of Excellence for Energy and Information Polymer Materials, South China University of Technology, Guangzhou 510640, China.
*Corresponding author. Email: zhiweilin@scut.edu.cn
†These authors contributed equally to this work.

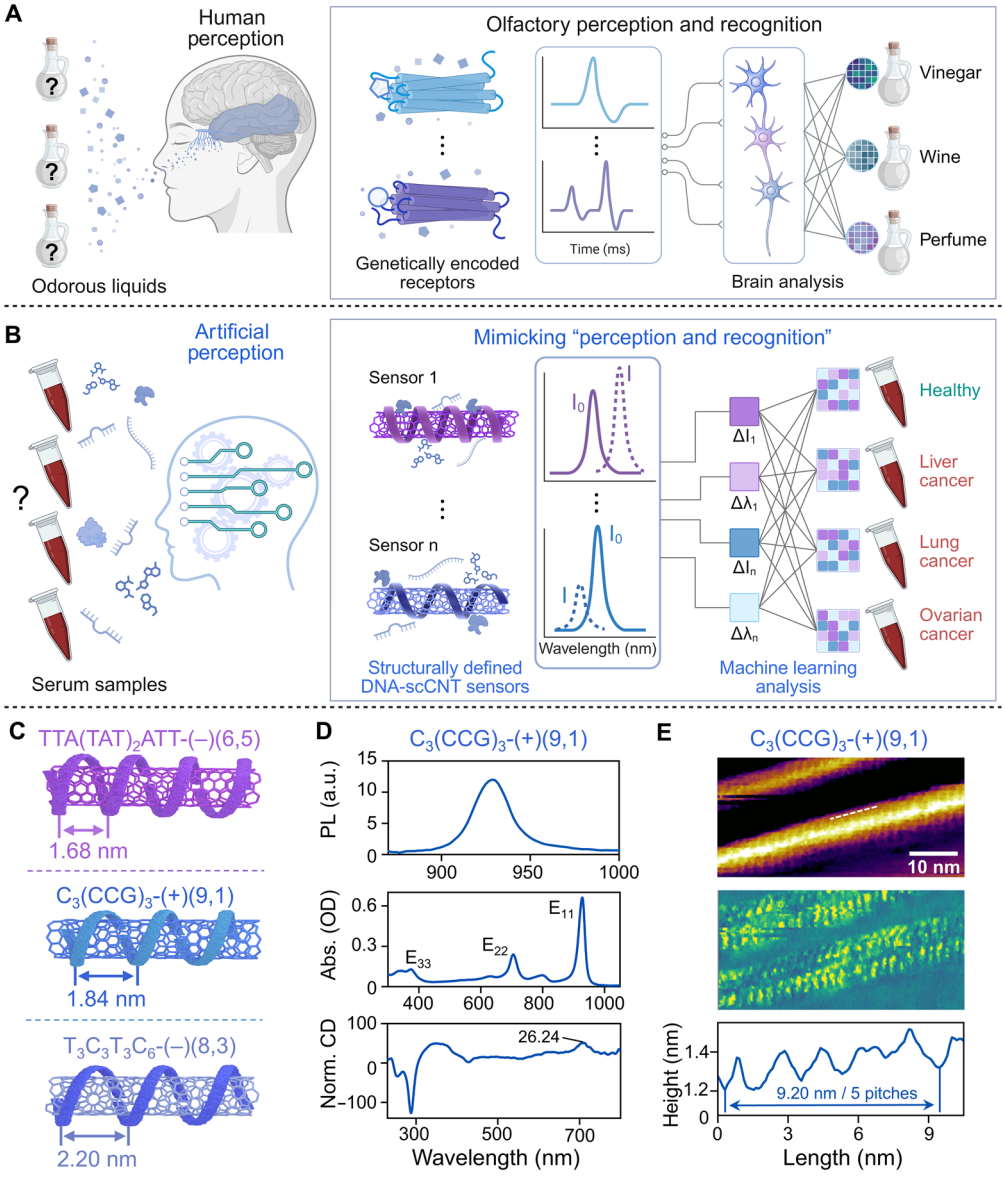

Fig. 1. APS for cancer detection. (**A**) Working principle of the human olfactory perception. Upon exposure to odorant molecules, olfactory receptors generate perceptual signals, which are interpreted by brain for odor recognition. (**B**) Working principle of the APS. Upon exposure to serum from different cohorts, DNA-scCNT sensors produce cohort-specific fingerprint optical responses, which are decoded by ML models for disease recognition. (**C**) Schematic illustration of three representative DNA-scCNTs used to construct sensor arrays. Each nanotube is wrapped with its resolving DNA sequence, forming a distinct, ordered wrapping conformation. (**D**) Photoluminescence (PL), absorption, and circular dichroism (CD) spectra of a representative sensor, $C_3(CCG)_3$-(+)(9,1). Spectral data for other sensors are provided in fig. S1. (**E**) AFM height (top), phase (middle) images, and pitch measurement (bottom) of $C_3(CCG)_3$-(+)(9,1).

resolving DNA sequence (Fig. 1, C and D, and fig. S1). These DNA strands adopt periodically ordered conformations with distinct and well-defined helical pitches (*33*), as exemplified by the atomic force microscopy (AFM) measurements of the $C_3(CCG)_3$-(+)(9,1) (Fig. 1E). The ordered DNA wrapping, coupled with the specific nanotube chirality, imparts a unique binding affinity for analytes, thereby enhancing the ability of DNA-scCNT sensors to differentiate analytes (*33*). Each sensor exhibits narrow, characteristic absorption and photoluminescence (PL) spectra, enabling the highly sensitive, high-resolution detection of minute environmental changes (*34*). The six-sensor panel provides multiplexed readouts that characterize serum samples from diverse physiological status, generating robust signature patterns (i.e., fingerprints) indicative of diseases state.

Analysis of sensing response datasets

We measured the PL spectral responses of the six sensors to serum samples collected from patients with three highly lethal malignancies: LC, LuC, and OC, as well as from NC individuals. As illustrated in Fig. 2A, the (8,3) sensor displayed distinct PL spectral responses to the four cohorts of samples. Compared to the baseline spectrum, both LC and NC serum resulted in PL enhancement, with NC exhibiting a more pronounced increase. Exposure to LuC and OC

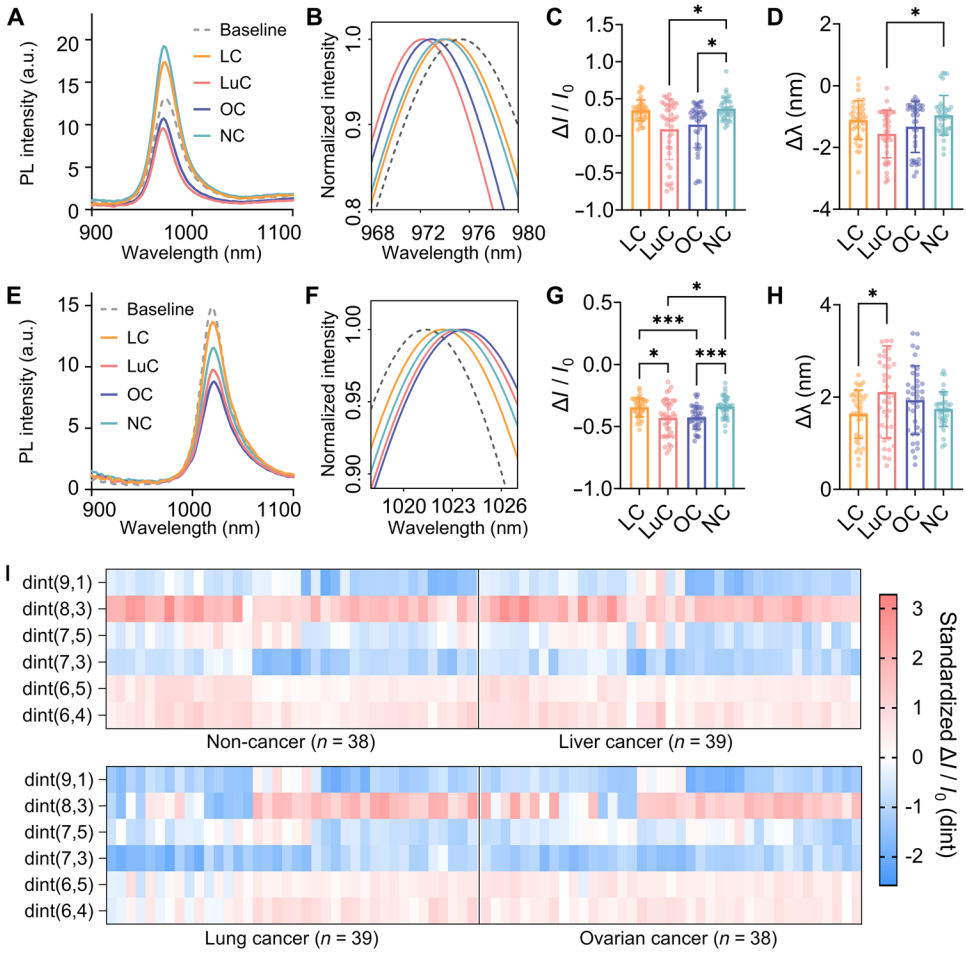

Fig. 2. Optical responses of DNA-scCNT sensors to various cancer and noncancer serum specimens. (A to D) for $T_3C_3T_3C_6$-(−)(8,3) and (E to H) for $C_2(GCCCC)_2$-(+)(7,3). (**A** and **E**) Representative PL spectra of $T_3C_3T_3C_6$-(−)(8,3) and $C_2(GCCCC)_2$-(+)(7,3) treated with liver cancer (LC), lung cancer (LuC), ovarian cancer (OC), and noncancer (NC) serum. The PL spectra of sensors in 20 v/v% fetal bovine serum (FBS) was used as the baseline. (**B** and **F**) Normalized PL spectra in (A) and (E), highlighting peak shifts. (**C** and **G**) Statistical analysis of relative PL intensity modulations ($\Delta I / I_0$) and (**D** and **H**) wavelength shifts ($\Delta\lambda$), treated with 154 serum samples from four cohorts ($n_{LC} = 39$, $n_{LuC} = 39$, $n_{OC} = 38$, and $n_{NC} = 38$). Bar heights and error bars represent mean ± SD across each cohort and each data point represents the mean of three replicate measurements. Statistical significance: $^*P < 0.05$, $^{**}P < 0.01$, and $^{***}P < 0.001$ (two-tailed tests). (**I**) Heatmaps of standardized PL intensity modulations (dint) for six DNA-scCNT sensors treated with 154 serum samples.

serum resulted in PL quenching, with the LuC sample inducing a more pronounced reduction. In addition, the PL peaks exhibited various degrees of blue shifts ranging from 1.0 to 3.1 nm after serum treatment (Fig. 2B). In contrast to (8,3), we observed distinctly different spectral patterns in the (7,3) sensor (Fig. 2E). All four samples triggered quenching effects on the PL intensity, with varying degrees of quenching. Meanwhile, the serum-induced peak shifts exhibited a trend opposite to that of the (8,3) sensor, with red shifts ranging from 1.0 to 2.3 nm (Fig. 2F). Representative responses of the other four sensors are shown in fig. S3. These distinct sensor responses from individuals in each group contribute to the construction of unique fingerprint profiles for specific cohorts. In contrast, chirality-mixed DNA-CNT sensors displayed severe spectral overlap and an indistinguishable response across four cohorts (fig. S4), highlighting the importance of our chirality-purified sensors in developing APS.

To ensure that these observed response differences are systematic, we performed statistical analysis on sensor array datasets from 154 serum samples ($n_{LC} = 39$, $n_{LuC} = 39$, $n_{OC} = 38$, and $n_{NC} = 38$). Two spectral variables were calculated: relative PL intensity changes $(I - I_0)/I_0$ ($\Delta I/I_0$) and peak shifts $\lambda - \lambda_0$ ($\Delta\lambda$). The results of significance tests for the (8,3) and (7,3) sensors are shown in Fig. 2, C and D and G and H, while the data for the remaining four sensors are presented in fig. S5. Statistically notable differences in sensor responses, with distinct patterns for each sensor, were observed across four cohorts. This indicates that each sensor contributes uniquely to sample discrimination. For instance, the (8,3) sensor demonstrated marked differences between LuC versus NC and OC versus NC (Fig. 2, C and D), while the (7,3) sensor revealed more pairs with notable differences (Fig. 2, G and H). Notably, the LC-LuC and LC-OC pairs, indistinguishable by (8,3), can be differentiated by (7,3). These distinct spectral responses offer valuable information for multicategory differentiation. However, individual sensors cannot statistically distinguish all four cohorts, necessitating a holistic sensor array analysis. This mirrors the human olfactory system, where individual receptors alone cannot identify specific scents, but collective responses of multiple receptors enable discrimination.

We then integrated the responses from each sensor to create the fingerprints for each cohort. To this end, we standardized the two spectral variables (dint and dwl) collected from 154 samples using *Z*-score normalization (Fig. 2I and fig. S6). The resulting heatmaps revealed differences across the four cohorts; however, analyzing them effectively through visual inspection proves challenging. These spectral signatures exhibit intricate interdependencies and nuanced variations, requiring advanced analytical approaches capable of detecting these subtle yet discriminative patterns embedded within the high-dimensional data space.

Development of cancer detection models

We first conducted principal components analysis (PCA) to visualize the data structure (Fig. 3A). On the PC1-PC2 plane, the 95% confidence ellipses show partially shifted centroids but substantial overlap. The first two components captured only 44.7% of total variance (table S2), indicating that the sensor features are largely independent (fig. S7) and that projecting the data onto two-dimensions entails considerable information loss. We therefore proceeded with supervised models using the full feature set.

ML algorithms were developed to decode the fingerprints of four groups, thereby establishing an effective APS for intergroup discrimination. We evaluated seven candidate algorithms, including artificial neural networks (ANNs), random forest (RF), extreme gradient boosting (XGB), linear discriminant analysis (LDA), support vector machines (SVMs), logistic regression (LR), and decision trees (DT). On the basis of 12 features of six sensors, we implemented a one-versus-rest training scheme across all models. Hyperparameters for each algorithm were optimized through Bayesian optimization (*35*) (table S3), and model performance was assessed using both F1 scores and the area under the receiver operating characteristic curve (AUC), calculated from fivefold nested cross-validation (CV).

Our preliminary algorithm assessment revealed that ANN, RF, and XGB achieved higher F1 scores and AUC values than other algorithms (Fig. 3B and fig. S8). Detailed performance metrics are presented in fig. S9. We thus selected the three top algorithms for further refinement and optimization (figs. S10 to S12). Consequently, RF and XGB outperformed ANN (Fig. 3C), with mean F1 scores and AUC values of 0.83 or higher. Additional performance metrics validated the robust classification efficacy of RF and XGB (fig. S13), and highlighted their complementary nature: RF was superior in OC and NC recognition, while XGB excelled in LC and LuC detection (fig. S14). This complementarity prompted the development of an RF + XGB ensemble model, which outperformed both the individual RF and XGB algorithms (Fig. 3C).

To quantify the performance gains from our optimization strategy and monitor for overfitting, we conducted a systematic ablation

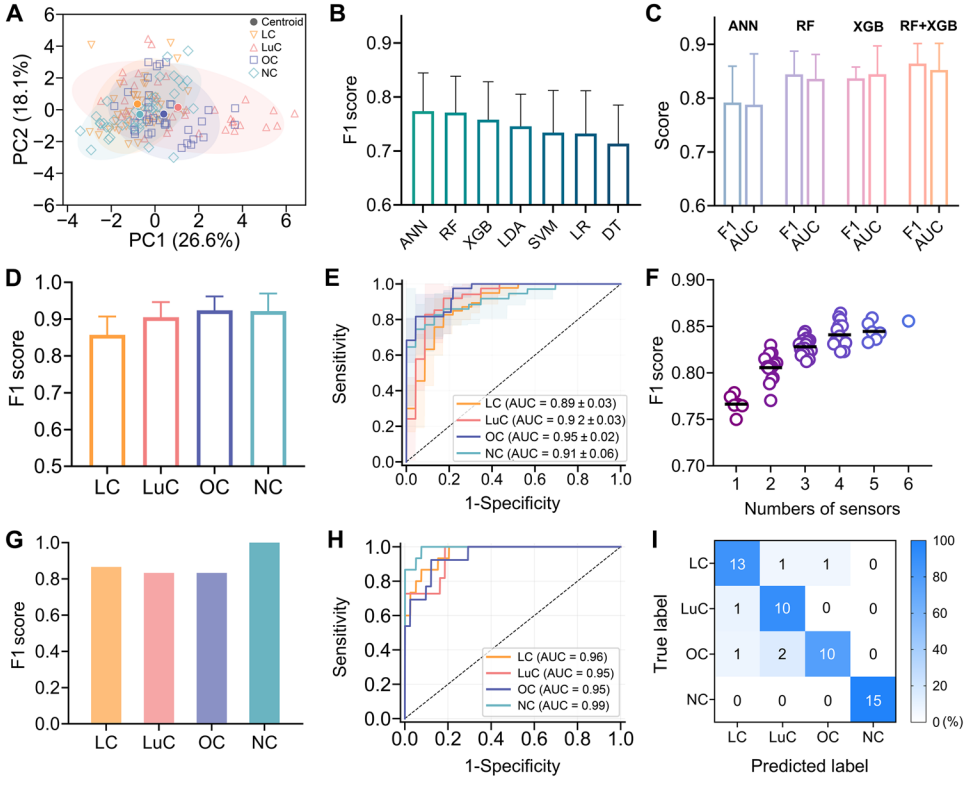

Fig. 3. Development of ML models for multicancer detection. (**A**) PCA of DNA-scCNTs sensor responses to 154 samples. Ellipses represent 95% confidence intervals (CIs). (**B**) Preliminary screening of seven algorithms based on F1 scores. (**C**) Performance metrics (F1 scores and AUC values) for refined individual algorithms (ANN, RF, and XGB) and the RF + XGB ensemble model. (**D**) Average F1 scores and (**E**) ROC curves for LC, LuC, OC, and NC classification using the refined RF + XGB ensemble model. (**F**) F1 scores achieved with varying numbers of sensor combinations using the ensemble model. Each point represents a specific sensor combination. In (B) to (F), data are presented as mean ± SD, derived from fivefold cross-validation (CV). (**G** to **I**) External validation on 54 samples ($n_{LC} = 15$, $n_{LuC} = 11$, $n_{OC} = 13$, and $n_{NC} = 15$) using the refined ensemble model: (G) F1 scores, (H) ROC curves with respective AUC values, and (I) confusion matrix, where the numbers indicate sample counts and the color scale represents accuracy percentages.

study. Removing engineered features led to a notable decline in the overall F1 score from 0.90 to 0.85 (fig. S15), confirming that the expanded feature space captures critical latent interactions inaccessible to raw features alone. Furthermore, while RF and XGB each performed robustly as standalone models, their ensemble consistently yielded notable improvements in both AUC and F1 score (fig. S16). This synergy validates our modeling approach, which effectively integrates the variance-reduction strengths of bagging with the bias-minimization efficiency of boosting.

Performance of APS in multicancer recognition

Given the superior performance of the RF + XGB ensemble, we further refined this model by optimizing both algorithm weights and hyperparameters to achieve better integration (fig. S17), and applied it to cancer classification. As shown in Fig. 3D, the model achieved impressive F1 scores for LC (0.86), LuC (0.91), OC (0.92), and NC (0.92), with reduced variance, indicating consistent performance across validation folds. Furthermore, the model demonstrated robust AUC metrics ranging from 0.89 to 0.95 across all categories (Fig. 3E). We then investigated the relationship between the feature set and model efficacy. The performance metrics consistently improved with the increasing number of sensors (Fig. 3F and fig. S18), and the permutation importance analysis (table S5) confirmed that all features contributed without redundancy, collectively demonstrating an optimal complexity-efficiency balance of our system. These results suggest that the APS is capable of simultaneously and efficiently recognizing multiple cancers.

To further assess the validity of the established APS, an external validation was conducted on 54 serum samples, including LC ($n = 15$), LuC ($n = 11$), OC ($n = 13$), and NC ($n = 15$). It achieved F1 scores of 0.87 (LC), 0.83 (LuC), 0.83 (OC), and 1.00 (NC) (Fig. 3G), along with AUC values of 0.96, 0.95, 0.95, and 0.99, respectively (Fig. 3H). These findings confirm the effective discrimination across different cohorts. Notably, the confusion matrix showed an overall accuracy of 88.9% [95% confidence interval (CI): 77.4 to 95.8%], with a sensitivity of 89% (95% CI: 79.3 to 96.4%) and a specificity of 96% (95% CI: 93.4 to 98.8%) (Fig. 3I and fig. S19). These external validation results further strengthen the feasibility of our APS for multicancer detection.

Detection mechanism of APS

To unravel the detection mechanism of APS, we implemented SHapley Additive exPlanations (SHAP) analysis (*36*). The SHAP summary plot systematically demonstrates how the value of each feature influences the model's output. Taking the classification of LC as an example, high values of the feature dint (7,3) strongly drove positive predictions for LC, whereas high values of dwl (9,1) opposed this classification (Fig. 4A). This pattern is further clarified in individual force plots. For a representative LC-positive sample, all features collectively produced a final SHAP value of 0.86, substantially higher than the baseline (0.288), resulting in the identification of LC (Fig. 4B). In contrast, for a non-LC case (Fig. 4C), the collective feature contributions yielded a SHAP value of 0.03, falling below the baseline and consequently leading to the classification of non-LC. The divergence in these outcomes is primarily driven by the distinct input values of key features, such as the lower dint (7,3) value in the non-LC case, which reduced the likelihood of LC classification. Additional results and discussion for the classification of other three cohorts are presented in fig. S20.

While correlating output results with input feature values sheds light on the APS decision-making mechanism, a more fundamental question remains: What is the biochemical basis for the specific fingerprints generated by the sensor array? To address this question, we collected the concentrations of 17 established tumor biomarkers (three for LC, seven for LuC, and seven for OC) from 146 patients with cancer and analyzed the correlation between these biomarker levels and the response of individual sensors using Spearman correlation analysis. This analysis revealed 13 groups of appreciable associations (fig. S21). For example, in LC samples, the level of carbohydrate antigen 19-9 (CA19-9) showed a negative correlation with the dint (6,5) feature (Fig. 4D). In LuC samples, a similar negative correlation was observed between neuron-specific enolase (NSE) and dint (8,3) (Fig. 4E). Additional examples for such correlations are shown in fig. S22. It is noteworthy that the same tumor markers could induce different optical responses across various diagnostic groups. For example, while alpha-fetoprotein (AFP) showed no observable correlation with any feature in LC samples, it exhibited distinct interaction patterns in OC specimens, with a positive correlation to dwl (9,1) (Fig. 4F) and a negative correlation to dwl (8,3) (fig. S22J). Similar context-dependent response was also observed for other markers, such as human chorionic gonadotropin-β (HCG-β; fig. S22, B to D, versus H) and NSE (fig. S22F versus Fig. 4E). These findings suggest that complex, group-specific serum microenvironments shape sensor-marker interactions that go beyond individual biomarkers, regulating the intergroup discrimination.

Titration experiments in pooled cancer serum matrices further validated the robustness and anti-interference capacity of these context-dependent signatures (fig. S23). In the LC cohort, for instance, the (6,5) sensor exhibited a notable concentration-dependent intensity decrease in response to CA19-9, a marker biologically linked to hepatic perturbations, while maintaining wavelength stability (fig. S23A), aligning with our Spearman correlation results. Crucially, clinically irrelevant markers for the respective cancer types elicited negligible or substantially attenuated responses compared to target-associated markers (fig. S23, B and C). This selective sensitivity underscores the ability of the APS to distinguish pathogenic signals from nonspecific molecular fluctuations within complex biological backgrounds.

We next used Mantel test to elucidate how the sensor array encodes serum samples among different diagnostic groups. Instead of analyzing each of tumor markers individually, they were treated collectively as representations of the serum microenvironment. By conceptualizing each serum sample as a point in multidimensional space, with each marker concentration defining a spatial coordinate, we explored the correlations between the overall serum environments and sensor responses. This analysis provides mechanistic insights into how the serum environment shapes sensor behavior, addressing the limitations of individual marker-sensor analyses. As illustrated in Fig. 4G, serum from the three cohorts demonstrated cohort-specific correlations. LC samples exhibited strong correlations with the features dint (9,1), dint (6,5), dint (6,4), dwl (7,5), dwl (6,5), and dwl (6,4), while LuC samples demonstrated distinct correlations with dint (9,1), dint (8,3), dint (7,3), and dint (6,5). Similarly, OC samples strongly correlated with dint (7,5), dint (6,4), dwl (8,3), and dwl (6,4). These distinct and sophisticated correlations between the features of sensor array and the biomarker panels encode the unique fingerprints for each diagnostic group. Notably, the feature heatmap in the right panel of Fig. 4G highlights the low interfeature correlations (with statistical significance and correlation

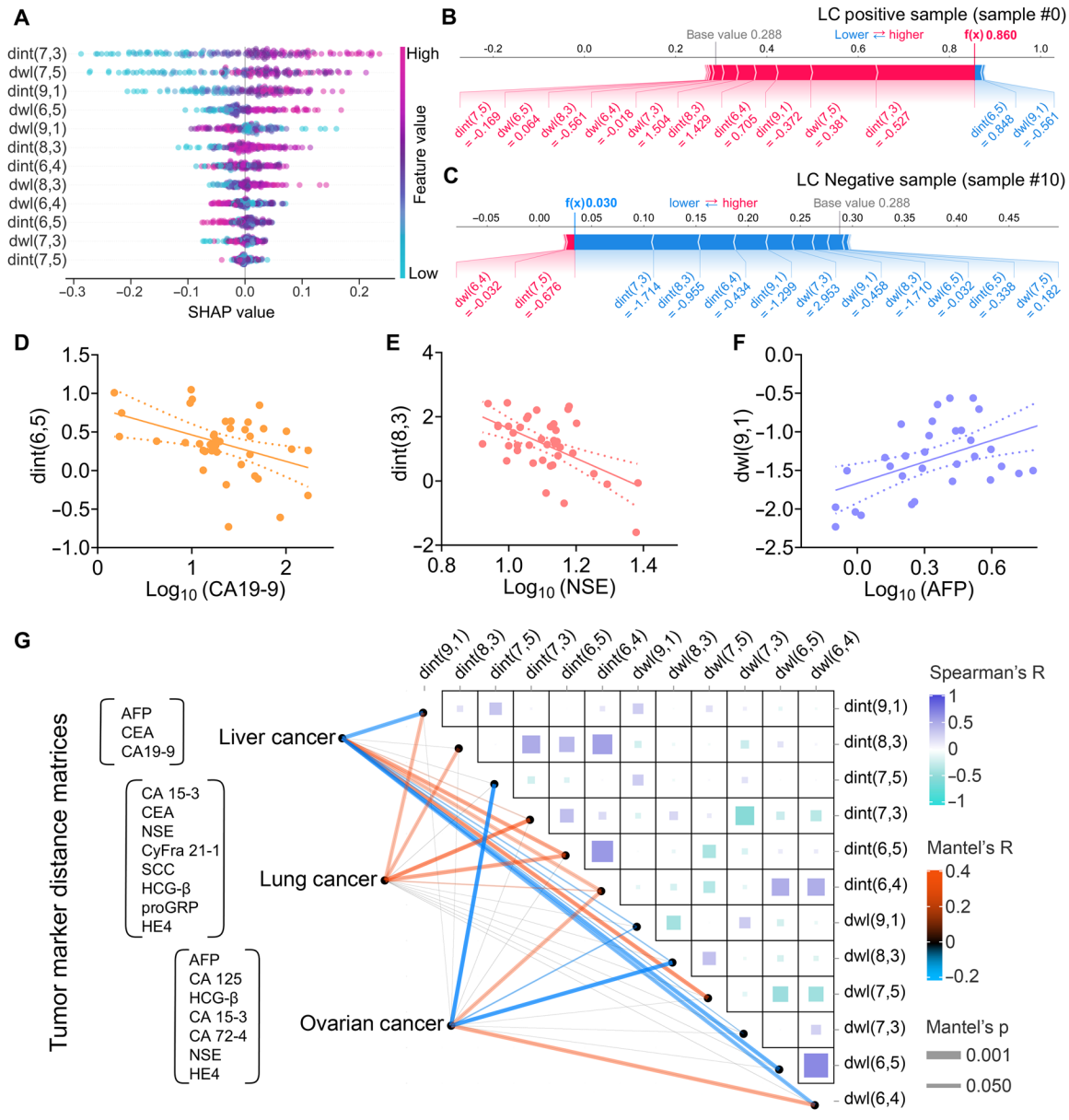

Fig. 4. Mechanism analysis of APS for cancer detection. (**A**) SHAP summary plot showing feature contributions in the LC classifier, with purple and cyan dots indicating higher and lower feature values, respectively. Features are ranked by importance from top to bottom, and the distribution patterns illustrate their impact on classification probability. (**B** and **C**) Force plots illustrating the influence of individual feature values on SHAP values and their contribution to final predictions in representative LC and non-LC samples. Red arrows indicate features driving predictions toward LC classification, whereas blue arrows show features opposing this classification. (**D** to **F**) Linear regression analysis between sensor features and tumor marker concentrations: (D) for CA 19-9 and dint (6,5) in LC, (E) for NSE and dint (8,3) in LuC, and (F) for AFP and dwl (9,1) in OC. Dashed lines indicate 95% CIs, and solid lines indicate regression fits. (**G**) Correlation analysis between tumor marker matrices and sensor features across cancer cohorts. Distance matrices (left) derived from cancer-specific tumor markers are correlated with each DNA-scCNT spectral response data via Mantel test. Line thickness indicates correlation significance; orange/blue represent positive/negative correlations. The heatmap (right panel) shows interfeature correlations of sensor responses, where color intensity indicates correlation magnitude and hue indicates direction.

values detailed in table S6), ensuring that the fingerprints of each diagnostic group are largely independent and, thus, distinguishable.

Individual biomarkers often have limited diagnostic accuracy for cancer due to their narrow representation of physiological status (*37*, *38*). In contrast, the APS uses DNA-scCNT arrays to detect a wide range of serum components, including both various established biomarkers and potentially unidentified cancer-associated substances (*29*). This method generates signature sensing patterns that more comprehensively represent the physiological status across different cohorts (*39*). These patterns are then interpreted by ML models, substantially improving diagnostic accuracy compared to traditional one-to-one recognition paradigms. This process is analogous to how human perceive and discriminate multiple stimuli.

Early-stage cancer detection by APS

Early-stage cancers are much more challenging to detect due to the small tumor size, minimal biomarker alterations, and subtle physiological changes. Detecting them using noninvasive biofluid-based methods presents a formidable challenge (*40*–*42*). We hypothesize that the APS may effectively capture these subtle differences in serum profiles, enabling the identification of incipient malignancies. To test this hypothesis, we applied the APS to detect early-stage cancer. Given the inherent scarcity of early-stage malignant samples, we focused on patients with LuC at early clinical stages (TNM ≤ stage I) for this study. However, we emphasize that our approach can be readily extended to other early-stage cancers, once sufficient samples become available. A total of 134 samples were used, including 36 early-stage LuC and 98 NC samples (53 from the established cohort and 45 from an additional cohort). Of these, 62 samples ($n_{\text{early-LuC}} = 24$; $n_{\text{NC}} = 38$) were allocated for model training, and the rest of 72 samples were used for independent external validation. Initial statistical analysis indicated notable differences in the optical response of sensors between early LuC and NC cohorts (Fig. 5A and fig. S24). However, PCA results show limited separability between the two cohorts (Fig. 5B), with the first two principal components accounting for only 40.2% of the total variance.

We reevaluated the established algorithms and identified an optimal RF + LDA ensemble model (fig. S25). This model demonstrated excellent performance in discriminating early-stage LuC from NC samples, achieving an average F1 score of 0.89, AUC of 0.93, sensitivity of 91%, and specificity of 92% in CV (Fig. 5C). External validation was conducted using an independent sample set comprising 12 early-stage LuC and 60 NC samples. This sample distribution presents a more challenging scenario for validating the effectiveness of APS, as it requires achieving high sensitivity for early-stage cancer detection, while simultaneously maintaining high specificity to minimize false positives among healthy individuals. Remarkable results were achieved, with an F1 score of 0.85, AUC of 0.94, sensitivity of 92% (95% CI: 61.5 to 99.8%), and specificity of 95% (95% CI: 86.1 to 99.0%) (Fig. 5D). The confusion matrix further illustrates the noteworthy outcomes (Fig. 5E). The overall accuracy reached 94% (95% CI: 86.4 to 98.5%), with a corresponding positive predictive value (PPV) of 79% (95% CI: 49.2 to 95.3%) and negative predictive value (NPV) of 98% (95% CI: 90.8 to 100.0%). These metrics demonstrate the APS's dual capability: identifying true early-stage LuC cases and reliably ruling out disease in negative results. We acknowledge that the real-world prevalence of early-stage LuC in general screening populations is substantially lower than the 1:5 ratio in this cohort, which would reduce PPV in practice. Nevertheless, the high NPV is expected to remain robust at lower disease prevalence. This positioning makes the APS a valuable tool for oncology screening workflows, particularly in high-risk populations where maximizing sensitivity and ensuring a reliable negative consensus are of primary clinical importance.

Clinical utility of APS

To evaluate the clinical utility of APS, we compared its performance with biofluid-based approaches for early-stage LuC detection (Fig. 5, F and G). The measured concentrations of LuC markers in most patients' serum fall below the reference thresholds recommended by

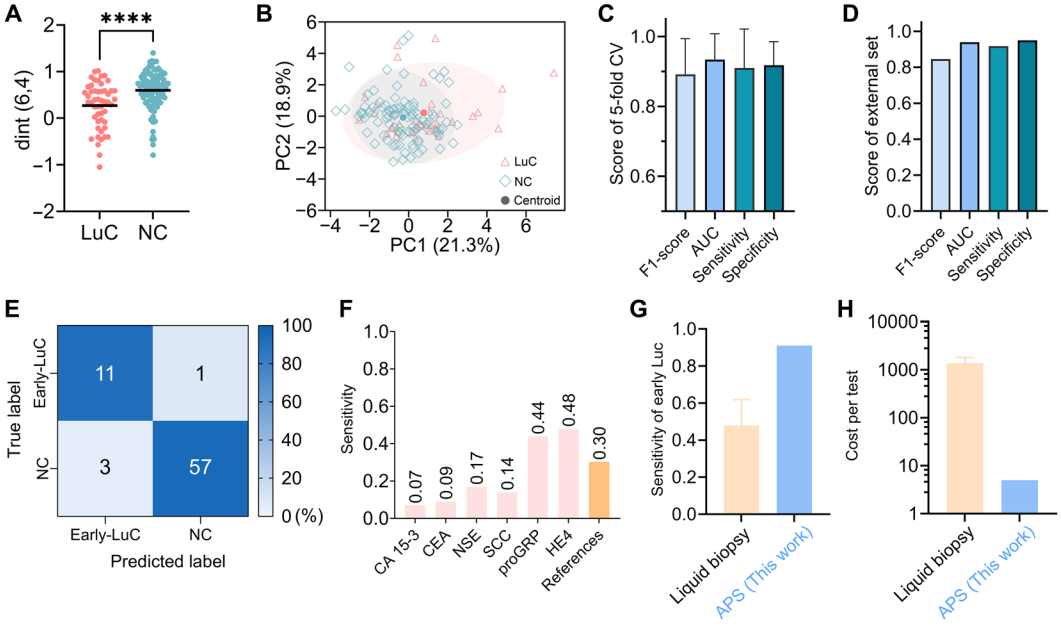

Fig. 5. Early-stage cancer detection. (**A**) Standardized PL intensity modulation in the representative (6,4) sensor for the early-stage LuC and NC groups. ****$P < 0.0001$ (two-tailed tests). (**B**) PCA of the early-stage LuC and NC groups, with 95% CIs shaded. The analyses in (A) and (B) were performed using data from 134 participants ($n_{\text{Early LuC}} = 36$ and $n_{\text{NC}} = 98$) with six DNA-scCNT sensors. (**C**) Performance metrics of the RF + LDA ensemble model, evaluated using fivefold nested CV on the training set ($n = 62$). (**D**) Performance of the RF + LDA model on the external validation cohort ($n = 72$) and (**E**) corresponding confusion matrix, where the numbers indicate sample counts and the color scale shows accuracy percentages. (**F**) Sensitivity of early-stage LuC detection based on the concentrations of individual tumor markers we measured (pink) and reported in the literature (orange), with clinical guideline-recommended cutoff values. (**G**) Sensitivity of early-stage LuC detection using our APS compared to other liquid biopsy methods reported in the literature. (**H**) Cost comparison of early-stage cancer screening using our APS and other liquid biopsy methods. Error bars represent SD.

clinical guidelines (table S7), leading to an overall sensitivity range of 7 to 48% (Fig. 5F, pink bars). This is consistent with the findings of a comprehensive literature review (*43*–*47*), which reported an average sensitivity of 30% for single biomarker screening in ≤ stage I LuC (Fig. 5F, orange bar). Current liquid biopsy approaches with established clinical utility typically achieve an average sensitivity of 50 to 60% at specificities above 90% (*43*–*47*), suggesting that a substantial proportion of positive cases remain undetected. While direct performance comparisons are inherently limited by differences in patient populations and study designs, the high sensitivity observed for APS at equivalent specificity suggests its potential to enhance diagnostic yield as a complementary modality (Fig. 5G).

Beyond analytical performance, we estimated the cost of cancer detection using APS to be approximately $4 USD per test (table S8). This is far lower than the current liquid biopsy techniques, such as ctDNA and DNA methylation sequencing, which typically cost around hundreds to thousands of dollars per test (Fig. 5H and table S8). Collectively, these attributes establish the APS as a promising, cost-effective, high-throughput candidate for accessible population-level screening programs.

In addition to its exceptional performance in multicancer and early-stage cancer detection, the APS is a highly modular platform, with DNA-scCNT sensing channels that can be easily modified and expanded, and ML models that can be continuously improved using state-of-the-art algorithms. This configurability facilitates the development of customized diagnostic solutions tailored to diverse clinical needs. Moreover, our method requires only 0.5 ml of serum for a complete analysis, rendering it highly amenable to integration into routine clinical screening protocols. This substantially enhances its clinical utility and potential for real-world applications.

DISCUSSION

In summary, we have developed a perception-based liquid biopsy platform that integrates structure-defined DNA-scCNT sensor arrays with ensemble ML models to accurately detect liver, lung, and ovarian cancers from serum. Notably, our strategy demonstrated exceptional performance in detecting early-stage cancers. Mechanistic analysis revealed that disease-specific fingerprints arise from differential fluorescence modulation of the sensor array in distinct serum milieux, shedding light on the biochemical basis underlying classification. Compared with existing liquid biopsy technologies, our strategy offers a high-performance, cost-effective, and streamlined alternative for early cancer detection. These improvements signify a paradigm shift in diagnostics, from the detection of isolated biomarkers to the systematic interpretation of holistic serum profiles.

Perception-based sensing is a compelling paradigm; by capturing integrated physiological patterns, it offers an untargeted strategy capable of detecting low-abundance signatures and uncharacterized disease-associated biomarkers that often evade conventional targeted assays. While previous success with defect-modified CNTs validated the feasibility of this approach, the transition to structurally defined DNA-scCNT sensors addresses the long-standing challenge of sensor heterogeneity. By ensuring each sensor species is characterized by a molecularly defined structure, we achieved robust multicancer discrimination within our study cohorts. This structural precision provides a foundational pathway for standardized quality control, a prerequisite for future clinical translation and cross-site reproducibility. Furthermore, the scalability of the DNA-scCNT platform offers a versatile framework for the potential incorporation of novel diagnostic indications.

While the current study establishes the APS as a robust platform, its transition into routine clinical practice necessitates further validation across several dimensions. First, the current cohort serves as an important proof-of-concept but requires expansion into larger, multicenter prospective studies to ensure generalizability across diverse and larger patient populations. Second, from a technical perspective, systematic assessments of calibration transfer and long-term inter-batch stability are essential to ensure performance consistency across different manufacturing lots and clinical environments. Last, moving beyond retrospective analysis to prospective clinical trials will be fundamental to establishing the real-world predictive utility and diagnostic validity of this sensing paradigm.

MATERIALS AND METHODS

Materials

CoMoCAT single-walled CNTs powders (tradename SG65i) were purchased from Sigma-Aldrich. Oligomers of single-stranded DNA were purchased from Sangon Biotech. Polyethylene glycol (PEG; molecular weight of 6 kDa, Alfa Aesar), potassium sodium tartrate tetrahydrate ($C_4H_{12}KNaO_{10}$, Sigama-Aldrich), disodium hydrogen phosphate (Na_2HPO_4), sodium dihydrogen phosphate (NaH_2PO_4), dipotassium hydrogen phosphate (K_2HPO_4), potassium dihydrogen phosphate (KH_2PO_4), sodium thiocyanate (NaSCN), sodium acetate (NaAc), and phosphate-buffered solution (PBS; 1 M, pH = 7.4), were all procured from J&K Scientific unless otherwise specified. Fetal bovine serum (FBS) was purchased from Gibco. CA19-9 (purified), HCG-β (purified), and AFP (purified) were purchased from Sangon Biotech.

Preparation of structurally defined DNA- scCNTs

DNA-CNT dispersions were prepared following previously reported procedures (*34*, *48*, *49*). SG65i CNT powders (1 mg) and DNA oligos (2.5 mg) were sonicated in 1-ml aqueous solution under different buffer conditions depending on the target CNT species: Sodium phosphate buffer (NaPB; 30 mM, pH = 4) was used for purifying $C_3(CCG)_3$-(+)(9,1), $C_2(GCCCC)_2$-(+)(7,3), and $(GGC)_2(GC)_3$-(−)(6,4); sodium chloride (NaCl, 30 mM) was used for $C_3GC_6GC_4$-(−)(7,5) and $TTA(TAT)_2ATT$-(−)(6,5); and NaPB (30 mM, pH = 7) was used for $T_3C_3T_3C_6$-(−)(8,3).

Structurally defined DNA-scCNTs were isolated through chirality-specific aqueous two-phase (ATP) extraction protocols. Specifically, (9,1), (7,3) and (6,4) chiralities were purified using a 7:3 PEG/Na^+ system. For other chiralities, the systems were adjusted as follows: (8,3) was extracted using a 7:3 PEG/Tar system; (7,5) was purified using a 7:3 PEG/K^+ system; and (6,5) was isolated using a 7:3 PEG/Tar system. The detailed formulations for these ATP systems are summarized below:

1) System 7:3 PEG/K^+: PEG 6 kDa [13.6 weight % (wt %)], K_2HPO_4 (8.8 wt %), KH_2PO_4 (4.84 wt %), and ultrapure water (72.76 wt %).

2) System 7:3 PEG/Na^+: PEG 6 kDa (12.3 wt %), $Na_2HPO_4{\cdot}7H_2O$ (12.2 wt %), $NaH_2PO_4{\cdot}H_2O$ (4.43 wt %), and ultrapure water (71.07 wt %).

3) System 7:3 PEG/Tar: PEG 6 kDa (18.2 wt %), $C_4H_{12}KNaO_{10}$ (19.4 wt %), and ultrapure water (62.4 wt %).

In a typical ATP separation, 3 volumes of DNA-CNT dispersions (60.0 μl) were mixed with 7 volumes of 7:3 stock solutions (140.0 μl). The mixtures were vortexed and subsequently centrifuged at 15,000*g*

for 3 min at room temperature to facilitate phase separation. The partitioned DNA-scCNTs in the top phase solution were collected, treated with 0.5 M NaSCN, and centrifuged to obtain the pellets, which were then redispersed in 10 mM PBS.

UV-vis-NIR absorption spectroscopy

Ultraviolet-visible–near-infrared (UV-vis-NIR) absorption spectra were collected on a Hitachi UH-5700 spectrophotometer from 200 to 1350 nm, using a 1 cm path length quartz microcuvette. All spectra were obtained with background subtraction.

PL spectroscopy

PL spectra were collected using a NS Super NanoSpectralyzer (Applied NanoFluorescence, Houston, TX) with an excitation wavelength of 660 nm. The spectra were recorded at room temperature.

CD spectroscopy

Circular dichroism (CD) measurements were performed on a Jasco J-1700 spectropolarimeter equipped with a 1-cm quartz cuvette. Spectral data were acquired across 780 to 200 nm wavelength range at 0.2 nm resolution with background correction.

Clinical serum samples

A total of 253 waste serum samples were obtained from diverse patient populations under a protocol approved by the Sun Yat-sen University Cancer Center Institutional Review Board (license number: B2025-104-01). Samples were collected between August 2023 and August 2025 in accordance with the Declaration of Helsinki. As this study used residual clinical specimens obtained from routine blood draws, involved no direct participant contact or intervention of any kind, and posed no greater than minimal risk to participants, informed consent was waived by the Institutional Review Board.

Cancer blood samples were drawn prior to any systemic treatment, surgery, or chemotherapy. LC cases ($n = 54$) were all primary hepatocellular carcinoma, confirmed by histopathological examination and classified by attending oncologists according to the China Liver Cancer staging system: stage Ia ($n = 9$), Ib ($n = 4$), IIa ($n = 5$), IIb ($n = 3$), IIIa ($n = 13$), and IIIb ($n = 11$); staging information was unavailable for nine cases. Sex distribution was 44 male and 10 female, with a median age of 54 years (range, 28 to 77). LuC cases ($n = 50$) comprised adenocarcinoma ($n = 35$), squamous cell carcinoma ($n = 11$), and other histological types ($n = 4$), spanning TNM stages IA1 through IIIB; 10 cases lacked explicit stage documentation in medical records. Sex distribution was 25 male and 25 female, with a median age of 64 years (range, 38 to 83). OC cases ($n = 51$) included high-grade serous carcinoma ($n = 11$), clear cell carcinoma ($n = 7$), endometrioid carcinoma ($n = 2$), granulosa cell tumor ($n = 2$), and other or histologically unspecified subtypes ($n = 29$), staged according to FIGO criteria from stage I through IVC. Median age was 51 years (range, 13 to 85). All diagnoses were established through comprehensive medical record review incorporating histopathological examination of biopsy or surgical specimens, validated by board-certified oncologists. Patients were excluded if they had a prior history of malignancy, concurrent autoimmune or inflammatory disease, active infection, or ongoing immunosuppressive therapy at the time of blood draw. Noncancer controls ($n = 98$) were enrolled based on negative results across hepatic and renal function tests, fasting glucose and lipid panels, and comprehensive tumor marker panels; individuals with any chronic systemic illness were excluded. Age distributions showed no statistically significant differences among groups [$P > 0.05$, one-way analysis of variance (ANOVA)]. Complete clinicopathological characteristics are summarized in table S9.

Sample collection followed standardized operating procedures: blood was drawn after overnight fasting into serum separator tubes, allowed to clot for 30 min at room temperature, then centrifuged at 3000*g* for 15 min at 4°C. Serum aliquots (500 μl) were stored at −80°C within 2 hours of collection, with no more than three freeze-thaw cycles before analysis.

Serum tumor biomarker assays

The concentrations of tumor biomarkers in serum were determined using the Roche cobas 801 analyzers with electrochemiluminescence immunoassay technology. The analyzer was used to quantify cancer antigen 15-3 (CA15-3), carcinoembryonic antigen (CEA), cytokeratin fragment 21-1 (CyFra21-1), squamous cell carcinoma antigen (SCC), HCG-β, pro-gastrin–releasing peptide (ProGRP), human epididymis protein 4 (HE4), AFP, cancer antigen 19-9 (CA19-9), cancer antigen 125 (CA125), cancer antigen 72-4 (CA72-4), and NSE, according to standardized manufacturer protocols.

Sensing assays of serum using DNA-scCNTs

Purified DNA-scCNT sensors were diluted with 10 mM PBS to prepare working solutions. The concentration of six sensors was specifically adjusted to a final optical density (OD) of 0.3. The sensors included: $(GGC)_2(GC)_3$-(−)(6,4), $TTA(TAT)_2ATT$-(−)(6,5), $C_2(GCCCC)_2$-(+)(7,3), $C_3GC_6GC_4$-(−)(7,5), $T_3C_3T_3C_6$-(−)(8,3), and $C_3(CCG)_3$-(+)(9,1).

For the sensing assays, 25 μl of patient serum samples were mixed with 100 μl of DNA-scCNT solutions (v/v = 1:4). FBS controls were prepared using the same protocol with DNA-scCNTs to establish baseline spectra. The comparison between serum-treated and FBS-treated spectra enabled the construction of feature vectors, which were used to differentiate serum samples from various diagnostic groups. All samples were prepared in triplicate and incubated for 24 hours at 25°C with agitation at 60 rpm using a THZ-98C shaking incubator (Shanghai Yiheng Scientific Instruments). After incubation, both PL and absorption spectra of all samples were collected.

Training/testing dataset construction

Sensor optical response data were obtained through Lorentzian fitting of DNA-scCNT PL spectra, capturing the following two features: E_{11} peak intensity and E_{11} peak wavelength. The mean values from triplicate measurements were used as feature data for ML analysis. Feature values were defined as the differential responses between patient sera and FBS controls.

Specifically, we quantified the optical response using two primary features: the E_{11} peak wavelength shift ($\Delta\lambda$) and the normalized intensity change ($\Delta I/I_0$). The wavelength shift was defined as $\Delta\lambda = \lambda - \lambda_0$, where λ and λ_0 represent the peak emission wavelengths in the serum sample and the FBS reference, respectively. Similarly, the intensity feature was expressed as $\Delta I = I - I_0$, where I and I_0 denote the corresponding peak intensities.

To eliminate potential batch effects arising from variations in sample collection timeframes and possible instrumental baseline drift, Z score standardization was applied to the data within each temporal batch (typically within 3 months from sample collection to assay completion). The standardized $\Delta I/I_0$ and $\Delta\lambda$ values were designated as

dint and dwl, respectively. This standardization also improved the convergence speed of ML models during training.

Statistical analysis

Statistical analyses were performed using GraphPad Prism 10.4 (GraphPad Software, San Diego, CA). To compare sensor response (dint and dwl values) across diagnostic groups, we implemented a stepwise statistical testing approach. Normality was assessed using the Shapiro-Wilk test, which is optimal for small-to-moderate sample sizes ($n = 40$ to 60 per group). For normally distributed data, variance homogeneity was evaluated using the Brown-Forsythe test. If both normality and homoscedasticity assumptions were met, one-way ANOVA was applied; otherwise, Welch's ANOVA was used for heterogeneous variances. For nonnormally distributed data, the nonparametric Kruskal-Wallis test was used. Post-hoc pairwise comparisons were conducted using Tukey's multiple comparisons test (following ANOVA) or Dunn's multiple comparisons test (following Kruskal-Wallis). All tests were two-tailed, with statistical significance level set at $\alpha = 0.05$.

Multicancer detection model development and validation

Algorithm selection and optimization

We systematically evaluated seven well-established ML algorithms for multicancer classification: LDA, LR, SVM, ANN, DT, RF, and XGB. On the basis of initial assessment, the top three algorithms were selected for further optimization and ensemble model development.

To ensure robust and unbiased performance estimation, we implemented a nested CV strategy with fivefold outer and fivefold inner loops. The outer loop assessed model generalization, while the inner loop optimized hyperparameters using Bayesian optimization with 10 initialization points and 60 iterations (BayesOpt package) within predefined space (table S3) to maximize the F1 score. Decision thresholds were dynamically optimized on validation sets within a range of 0.1 to 0.7 in 0.025 increments to maximize model performance.

Model performance was evaluated using multiple metrics: F1 score, AUC, sensitivity, and specificity. Given the four-class discrimination task (LC, LuC, OC, and NC), final predictions were determined by selecting the class with the highest confidence score from all four binary classifiers.

All ML analyses were conducted in Python 3.11 with the following libraries: NumPy 1.24 for numerical computations, pandas 2.1 for data manipulation, scikit-learn 1.1 for ML algorithms (LDA, LR, SVM, ANN, DT, and RF), and XGBoost 2.0 for XGB. These versions were maintained consistently throughout all modeling experiments to ensure reproducibility.

Advanced model optimization

The three top-performing algorithms (RF, XGB, and ANN) were systematically optimized through a three-stage pipeline.

Stage 1: Feature engineering. To enhance intergroup discrimination and capture complex sensor interactions, we used three complementary feature generation methods: (i) polynomial features with second-order interactions and squared terms; (ii) pairwise ratio features derived from sensor responses; and (iii) Gaussian kernel-based interactions including radial basis function pairwise similarities, weighted Gaussian combinations, distance features, and local density estimates. These methods expanded the feature space from 12 original sensor measurements to over 100 engineered features. To accommodate the expanded feature space and prevent the curse of dimensionality, we performed iterative optimization of hyperparameters and feature dimensionality (corresponding to iterations 1 to 8 in figs. S10 to S12), and identified Gaussian kernel interactions with 30 to 45 features as the optimal configuration, achieving both stable and superior performance. This feature set was subsequently refined through algorithm-specific feature selection.

Stage 2: Feature selection optimization. Two selection strategies were evaluated (iterations 9 and 10 in figs. S10 to S12): mutual information (*50*) and the Boruta algorithm (*51*). The optimal configurations were identified as follows: ANN with Boruta (35 features), RF with Boruta (40 features), and XGB with mutual information (40 features).

Stage 3: Data augmentation. To mitigate the inherent class imbalance resulting from OvR decomposition and prevent prediction bias toward the majority classes, we implemented data augmentation using two techniques: synthetic minority oversampling technique (*52*) and adaptive synthetic sampling (*53*) (iterations 11 and 12 in figs. S10 and S12). These techniques generated synthetic samples for the minority classes, ensuring balanced training sets while maintaining the original data distribution characteristics. The optimal hyperparameter space for each algorithm determined through systematic optimization is summarized in table S4.

Ensemble model development

Following individual algorithm optimization, we developed an ensemble model by combining the top-performing RF and XGB algorithms. Initially, these two individual algorithms with the highest CV performance were integrated using equal weights (50% each). Subsequently, the model weights were fine-tuned via Bayesian optimization (iteration 2 in fig. S17) to achieve an enhanced ensemble that leveraged the strengths of each individual model. The ensemble's expanded hyperparameter space, nearly twice as large as that of individual models, presented multiple local optima that challenged conventional Bayesian optimization. To address this increased complexity, we used two advanced optimization strategies: the tree-structured Parzen estimator (TPE) via Optuna framework (*54*) and a genetic algorithm (GA) (*55*), corresponding to iterations 3 to 6 in fig. S17. TPE optimization was performed with 15 initialization points and 60 total trials. GA used a population size of 50 over 60 generations, with crossover rate 0.8, mutation rate 0.125, elite ratio 0.125, and tournament size 3. Both strategies explored the high-dimensional parameter space more effectively than the standard Bayesian optimization. Last, the optimized ensemble model was evaluated on an independent external test set, with performance metrics, including F1 score, sensitivity, specificity, and confusion matrix analysis, providing unbiased assessment of model generalizability.

Permutation feature importance

Permutation feature importance was used to quantify individual sensor contributions to the optimized RF + XGB ensemble model. For each of the 12 original features (dint and dwl from six DNA-scCNTs), we assessed the decrease in model performance when feature-target relationships were disrupted. Specifically, for each feature, values were randomly shuffled across samples while preserving other features, and the ensemble predictions were recalculated using the optimized weights. Feature importance was quantified as the decrease in AUC score between the baseline and permuted performance. This permutation process was repeated 20 times per feature to ensure statistical stability, with the final importance score calculated as the mean AUC degradation.

SHAP analysis

To interpret the decision-making logic of the optimized ensemble model, we performed SHAP analysis. Given the heterogeneous nature of the RF + XGB ensemble architecture, we used the model-agnostic KernelExplainer (*56*) to quantify the attribution of individual sensor features to the final classification. The explainer was implemented using the SHAP Python library with default parameterization, including an identity link function and automated sample size determination.

A background dataset of 100 representative samples was generated via stratified random sampling from the training set. This dataset approximates the expected model output and serves as the baseline (base value) for the additive explanations. SHAP values were then computed for each feature of every sample, independently for each of the four diagnostic classes. These values quantify the positive or negative contribution of each feature in pushing the model's output from the baseline to its final prediction for a specific class.

Global feature importance was determined by calculating the mean absolute SHAP value for each feature across all samples and classes. This global ranking was visualized using SHAP summary plots, which illustrate the distribution, magnitude, and direction of feature impacts. For local interpretability, force plots were generated for representative, correctly classified samples. These plots depict the direction and magnitude of each feature's contribution, and how these contributions accumulate to influence the model's output, providing insights into the rationale behind individual predictions. For example, they explain why a specific sample was classified as a true positive for LC, while simultaneously providing a reliable negative consensus for LuC, OC, and NC.

Spearman correlation analysis

To evaluate the relationship between known serum tumor markers and DNA-scCNT spectral responses, Spearman rank correlation analysis was performed using scipy 1.1. The analysis encompassed three cancer types with their respective biomarker panels: LC (AFP, CEA, and CA19-9), LuC (CA15-3, CEA, NSE, CyFra21-1, SCC, HCG-β, and ProGRP, HE4), and OC (AFP, CA-125, HCG-β, CA15-3, CA72-4, NSE, and HE4). Biomarker concentrations were log10-transformed to reduce skewness, and each transformed biomarker was correlated with the 12 DNA-scCNT spectral features (dint and dwl values for six sensors).

Correlation coefficients and *P* values were calculated for biomarker-sensor pairs with complete data (minimum $n = 10$). Statistical significance was classified as: $***P < 0.001$, $**P < 0.05$, and $*P < 0.1$. Benjamini-Hochberg false discovery rate (FDR) correction was applied for multiple comparisons. The results were visualized using correlation heatmaps with a custom diverging colormap and significance annotations. To ensure statistical validity, analyses excluded samples with missing biomarker data.

Mantel test analysis

To assess the overall association between the serum biochemical environment and individual DNA-scCNT spectral responses, we used the known tumor marker levels for each cancer type as a holistic representation of the disease-specific serum profile. Mantel test analysis was performed using scipy.spatial.distance (version 1.9.0) (*57*, *58*). For each cancer type, pairwise Euclidean distance matrices were computed separately for both biomarker concentrations and DNA-scCNT spectral features. The biomarker panels included LC (AFP, CEA, and CA19-9), LuC (CA15-3, CEA, NSE, CyFra21-1, SCC, HCG-β, and ProGRP, HE4), and OC (AFP, CA-125, HCG-β, CA15-3, CA72-4, and NSE, HE4).

In a typical computational example, for n LC samples, a biomarker distance matrix was constructed by calculating Euclidean distances between all possible sample pairs based on their three-dimensional biomarker vectors (e.g., hypothetical sample A: [AFP, CEA, CA19-9] = [12.3, 8.7, 45.2] ng/ml versus sample B: [15.8, 12.1, 52.7] ng/ml versus sample C: [8.9, 6.2, 38.4] ng/ml, etc.), resulting in an $n \times n$ symmetric distance matrix. For each CNT spectral parameter, a corresponding single-feature distance matrix was computed from the same samples. The upper triangular elements from both distance matrices were extracted as vectors, and their Spearman correlation coefficient was calculated to quantify the association between the biomarker profile and individual spectral feature.

Distance matrices were computed using the pdist function with Euclidean metric and then converted into square matrices via squareform. Mantel correlation coefficients were calculated as Spearman correlations between the upper triangular elements of corresponding distance matrices. Statistical significance was assessed through permutation testing with 9999 random permutations. Samples with missing biomarker data were excluded through complete case deletion to maintain statistical validity. This analysis resulted in 12 independent Mantel correlations for each cancer type (one per CNT spectral feature). Visualization was performed using OmicShare (https://omicshare.com), generating a network heatmap that displayed both Spearman correlation coefficients and Mantel test results, with significance thresholds at $P < 0.05$ and $P < 0.001$ (Benjamini-Hochberg FDR-adjusted).

Single-analyte titration and anti-interference assays

Tumor markers CA19-9, AFP, and HCG-β were reconstituted in PBS and serially diluted 10-fold from a stock concentration of 100 to 0.1 μg/ml (for CA19-9, diluted from 10,000 to 10 U/ml). To evaluate anti-interference performance, a 15-μl aliquot of each marker solution was spiked into 35 μl of pooled cancer serum (comprising equal volumes from five donors of the respective LC, LuC, or OC cohorts). Subsequently, 100 μl of (6,5), (9,1), or (7,5) sensors at 0.3 OD were added to serum-marker mixture. All samples were prepared in triplicate and incubated at 25°C with shaking. PL spectra were acquired using the same instrumental settings and data processing workflow as described above.

Early-stage cancer detection model development and validation

Algorithm selection and optimization

To apply our APS for early-stage cancer detection, we selected early-stage LuC and healthy control samples from our dataset, incorporating 45 additional healthy samples, to develop a detection model. We evaluated the same seven ML algorithms using identical hyperparameter space (table S3), Bayesian optimization strategies, and five-fold nested CV, as described in the multicancer detection framework. On the basis of CV performance, RF and LDA were identified as the top-performing algorithms for further development.

Advanced model optimization

Given LDA's limited hyperparameter space, optimization efforts focused on RF model enhancement using the same hyperparameter tuning strategies described above. We applied the Gaussian kernel feature engineering approach established in the multicancer framework, expanding 12 sensor measurements to over 100 features, followed

by Boruta-based feature selection to identify 40 optimal features. Unlike the multicancer model, the relatively balanced training dataset (early-stage LuC = 24 and NC = 38) eliminated the need for data augmentation.

Ensemble model development

The optimized RF and LDA models were integrated using Optuna-based optimization with TPE sampling (100 trials), simultaneously optimizing the ensemble hyperparameter space and model weights to maximize the performance metrics. External validation was conducted using an independent set of samples (early-stage LuC = 12 and NC = 60). To adapt to new base rates of cancer in the data, we implemented a fine-tuning approach (*27*, *59*): A separate calibration set of 10 samples independent of the external validation set was used to synthesize data via multivariate Gaussian sampling (noise range: 0.05 to 0.20, multiplier = 5), creating an isolated fine-tuning set for decision threshold optimization. The ensemble model was then evaluated on the independent external validation set of 72 samples. No samples from this validation set were involved in any phase of model training, feature selection, or threshold tuning.

Supplementary Materials

This PDF file includes:

Figs. S1 to S25
Tables S1 to S9
References

REFERENCES

1. J. C. M. Wan, P. Sasieni, N. Rosenfeld, Promises and pitfalls of multi-cancer early detection using liquid biopsy tests. *Nat. Rev. Clin. Oncol.* **22**, 566–580 (2025).
2. L. Ma, H. Guo, Y. Zhao, Z. Liu, C. Wang, J. Bu, T. Sun, J. Wei, Liquid biopsy in cancer: Current status, challenges and future prospects. *Signal Transduct. Target. Ther.* **9**, 336 (2024).
3. M. Ignatiadis, G. W. Sledge, S. S. Jeffrey, Liquid biopsy enters the clinic — Implementation issues and future challenges. *Nat. Rev. Clin. Oncol.* **18**, 297–312 (2021).
4. M. K. Masud, J. Na, M. Younus, M. S. A. Hossain, Y. Bando, M. J. A. Shiddiky, Y. Yamauchi, Superparamagnetic nanoarchitectures for disease-specific biomarker detection. *Chem. Soc. Rev.* **48**, 5717–5751 (2019).
5. X. Chen, Y. Ba, L. Ma, X. Cai, Y. Yin, K. Wang, J. Guo, Y. Zhang, J. Chen, X. Guo, Q. Li, X. Li, W. Wang, Y. Zhang, J. Wang, X. Jiang, Y. Xiang, C. Xu, P. Zheng, J. Zhang, R. Li, H. Zhang, X. Shang, T. Gong, G. Ning, J. Wang, K. Zen, J. Zhang, C. Y. Zhang, Characterization of microRNAs in serum: A novel class of biomarkers for diagnosis of cancer and other diseases. *Cell Res.* **18**, 997–1006 (2008).
6. R. Lawrence, M. Watters, C. R. Davies, K. Pantel, Y. J. Lu, Circulating tumour cells for early detection of clinically relevant cancer. *Nat. Rev. Clin. Oncol.* **20**, 487–500 (2023).
7. K. L. Diehl, E. V. Anslyn, Array sensing using optical methods for detection of chemical and biological hazards. *Chem. Soc. Rev.* **42**, 8596–8611 (2013).
8. Y. Geng, W. J. Peveler, V. M. Rotello, Array-based "chemical nose" sensing in diagnostics and drug discovery. *Angew. Chem. Int. Ed. Engl.* **58**, 5190–5200 (2019).
9. C.-C. You, O. R. Miranda, B. Gider, P. S. Ghosh, I.-B. Kim, B. Erdogan, S. A. Krovi, U. H. F. Bunz, V. M. Rotello, Detection and identification of proteins using nanoparticle–fluorescent polymer 'chemical nose' sensors. *Nat. Nanotechnol.* **2**, 318–323 (2007).
10. M. Zheng, A. Jagota, M. S. Strano, A. P. Santos, P. Barone, S. G. Chou, B. A. Diner, M. S. Dresselhaus, R. S. McLean, G. B. Onoa, G. G. Samsonidze, E. D. Semke, M. Usrey, D. J. Walls, Structure-based carbon nanotube sorting by sequence-dependent DNA assembly. *Science* **302**, 1545–1548 (2003).
11. X. Tu, S. Manohar, A. Jagota, M. Zheng, DNA sequence motifs for structure-specific recognition and separation of carbon nanotubes. *Nature* **460**, 250–253 (2009).
12. M. Zheng, A. Jagota, E. D. Semke, B. A. Diner, R. S. McLean, S. R. Lustig, R. E. Richardson, N. G. Tassi, DNA-assisted dispersion and separation of carbon nanotubes. *Nat. Mater.* **2**, 338–342 (2003).
13. M. Zheng, Structure-defined DNA-carbon nanotube hybrids and their applications. *ECS Trans.* **85**, 511–517 (2018).
14. J. Zhang, M. P. Landry, P. W. Barone, J.-H. Kim, S. Lin, Z. W. Ulissi, D. Lin, B. Mu, A. A. Boghossian, A. J. Hilmer, A. Rwei, A. C. Hinckley, S. Kruss, M. A. Shandell, N. Nair, S. Blake, F. Şen, S. Şen, R. G. Croy, D. Li, K. Yum, J.-H. Ahn, H. Jin, D. A. Heller, J. M. Essigmann, D. Blankschtein, M. S. Strano, Molecular recognition using corona phase complexes made of synthetic polymers adsorbed on carbon nanotubes. *Nat. Nanotechnol.* **8**, 959–968 (2013).
15. S. Kruss, M. P. Landry, E. Vander Ende, B. M. A. Lima, N. F. Reuel, J. Zhang, J. Nelson, B. Mu, A. Hilmer, M. S. Strano, Neurotransmitter detection using corona phase molecular recognition on fluorescent single-walled carbon nanotube sensors. *J. Am. Chem. Soc.* **136**, 713–724 (2014).
16. P. W. Barone, S. Baik, D. A. Heller, M. S. Strano, Near-infrared optical sensors based on single-walled carbon nanotubes. *Nat. Mater.* **4**, 86–92 (2005).
17. G. Bisker, J. Dong, H. D. Park, N. M. Iverson, J. Ahn, J. T. Nelson, M. P. Landry, S. Kruss, M. S. Strano, Protein-targeted corona phase molecular recognition. *Nat. Commun.* **7**, 10241 (2016).
18. Z. Yaari, Y. Yang, E. Apfelbaum, C. Cupo, A. H. Settle, Q. Cullen, W. Cai, K. L. Roche, D. A. Levine, M. Fleisher, L. Ramanathan, M. Zheng, A. Jagota, D. A. Heller, A perception-based nanosensor platform to detect cancer biomarkers. *Sci. Adv.* **7**, eabj0852 (2021).
19. P. V. Jena, D. Roxbury, T. V. Galassi, L. Akkari, C. P. Horoszko, D. B. Iaea, J. Budhathoki-Uprety, N. Pipalia, A. S. Haka, J. D. Harvey, J. Mittal, F. R. Maxfield, J. A. Joyce, D. A. Heller, A carbon nanotube optical reporter maps endolysosomal lipid flux. *ACS Nano* **11**, 10689–10703 (2017).
20. T. V. Galassi, P. V. Jena, J. Shah, G. Ao, E. Molitor, Y. Bram, A. Frankel, J. Park, J. Jessurun, D. S. Ory, A. Haimovitz-Friedman, D. Roxbury, J. Mittal, M. Zheng, R. E. Schwartz, D. A. Heller, An optical nanoreporter of endolysosomal lipid accumulation reveals enduring effects of diet on hepatic macrophages in vivo. *Sci. Transl. Med.* **10**, eaar2680 (2018).
21. R. Nißler, O. Bader, M. Dohmen, S. G. Walter, C. Noll, G. Selvaggio, U. Groß, S. Kruss, Remote near infrared identification of pathogens with multiplexed nanosensors. *Nat. Commun.* **11**, 5995 (2020).
22. J. Zhang, A. A. Boghossian, P. W. Barone, A. Rwei, J. H. Kim, D. Lin, D. A. Heller, A. J. Hilmer, N. Nair, N. F. Reuel, M. S. Strano, Single molecule detection of nitric oxide enabled by $d(AT)_{15}$ DNA adsorbed to near infrared fluorescent single-walled carbon nanotubes. *J. Am. Chem. Soc.* **133**, 567–581 (2011).
23. J. D. Harvey, P. V. Jena, H. A. Baker, G. H. Zerze, R. M. Williams, T. V. Galassi, D. Roxbury, J. Mittal, D. A. Heller, A carbon nanotube reporter of microRNA hybridization events in vivo. *Nat. Biomed. Eng.* **1**, 0041 (2017).
24. D. A. Heller, H. Jin, B. M. Martinez, D. Patel, B. M. Miller, T.-K. Yeung, P. V. Jena, C. Höbartner, T. Ha, S. K. Silverman, M. S. Strano, Multimodal optical sensing and analyte specificity using single-walled carbon nanotubes. *Nat. Nanotechnol.* **4**, 114–120 (2009).
25. X. Gong, S.-Y. Cho, S. Kuo, B. Ogunlade, K. Tso, D. P. Salem, M. S. Strano, Divalent metal cation optical sensing using single-walled carbon nanotube corona phase molecular recognition. *Anal. Chem.* **94**, 16393–16401 (2022).
26. J. Ackermann, J. T. Metternich, S. Herbertz, S. Kruss, Biosensing with fluorescent carbon nanotubes. *Angew. Chem. Int. Ed. Engl.* **61**, e202112372 (2022).
27. C. Tian, S. Lee, S. Park, Y. Cho, C. Baek, S. Y. Cho, Decoding hidden features in near-infrared fluorescence spectra of single-walled carbon nanotubes via machine learning for multiplexed virus identification. *ACS Nano* **19**, 23992–24004 (2025).
28. M. Kim, C. Chen, Z. Yaari, R. Frederiksen, E. Randall, J. Wollowitz, C. Cupo, X. Wu, J. Shah, D. Worroll, R. E. Lagenbacher, D. Goerzen, Y.-M. Li, H. An, Y. Wang, D. A. Heller, Nanosensor-based monitoring of autophagy-associated lysosomal acidification in vivo. *Nat. Chem. Biol.* **19**, 1448–1457 (2023).
29. M. Kim, C. Chen, P. Wang, J. J. Mulvey, Y. Yang, C. Wun, M. Antman-Passig, H.-B. Luo, S. Cho, K. Long-Roche, L. V. Ramanathan, A. Jagota, M. Zheng, Y. Wang, D. A. Heller, Detection of ovarian cancer via the spectral fingerprinting of quantum-defect-modified carbon nanotubes in serum by machine learning. *Nat. Biomed. Eng.* **6**, 267–275 (2022).
30. D. Goerzen, M. Kim, C. Schroff, M. N. Hoang, J. S. Wollowitz, A. Kolb, J. P. Walshon, K. McCortney, C. Horbinski, K. Galbraith, S. Raoof, M. Snuderl, A. Ordureau, D. A. Heller, Machine perception liquid biopsy identifies brain tumours via systemic immune and tumour microenvironment signature. *Nat. Nanotechnol.* **21**, 277–287 (2026).
31. C.-Y. Su, K. Menuz, J. R. Carlson, Olfactory perception: Receptors, cells, and circuits. *Cell* **139**, 45–59 (2009).
32. C. Bushdid, M. O. Magnasco, L. B. Vosshall, A. Keller, Humans can discriminate more than 1 trillion olfactory stimuli. *Science* **343**, 1370–1372 (2014).
33. Y. Li, Y. Wen, L. C. Beltrán, L. Zhu, S. Tian, J. Liu, X. Zhou, P. Chen, E. H. Egelman, M. Zheng, Z. Lin, Understanding DNA-encoded carbon nanotube sorting and sensing via sub-nm-resolution structural determination. *Sci. Adv.* **11**, eadt9844 (2025).
34. J. Chen, Y. Li, J. Wu, J. Liu, X. Zhou, Z. Li, K. Tang, L. Shi, Z. Zhang, Z. Lin, Ordered DNA-wrapped single-chirality carbon nanotubes enable an unparalleled sensing platform for copper ion detection. *ACS Nano* **19**, 28743–28754 (2025).
35. R. van de Schoot, S. Depaoli, R. King, B. Kramer, K. Märtens, M. G. Tadesse, M. Vannucci, A. Gelman, D. Veen, J. Willemsen, C. Yau, Bayesian statistics and modelling. *Nat. Rev. Methods Primers* **1**, 1 (2021).
36. S. M. Lundberg, S.-I. Lee, "A unified approach to interpreting model predictions" in *Proceedings of the 31st International Conference on Neural Information Processing Systems* (Curran Associates, 2017), pp. 4768–4777.

37. A. Passaro, M. Al Bakir, E. G. Hamilton, M. Diehn, F. André, S. Roy-Chowdhuri, G. Mountzios, I. I. Wistuba, C. Swanton, S. Peters, Cancer biomarkers: Emerging trends and clinical implications for personalized treatment. *Cell* **187**, 1617–1635 (2024).
38. Y. Zhou, L. Tao, J. Qiu, J. Xu, X. Yang, Y. Zhang, X. Tian, X. Guan, X. Cen, Y. Zhao, Tumor biomarkers for diagnosis, prognosis and targeted therapy. *Signal Transduct. Target. Ther.* **9**, 132 (2024).
39. R. L. Pinals, D. Yang, D. J. Rosenberg, T. Chaudhary, A. R. Crothers, A. T. Iavarone, M. Hammel, M. P. Landry, Quantitative protein corona composition and dynamics on carbon nanotubes in biological environments. *Angew. Chem. Int. Ed. Engl.* **59**, 23668–23677 (2020).
40. D. Crosby, S. Bhatia, K. M. Brindle, L. M. Coussens, C. Dive, M. Emberton, S. Esener, R. C. Fitzgerald, S. S. Gambhir, P. Kuhn, T. R. Rebbeck, S. Balasubramanian, Early detection of cancer. *Science* **375**, eaay9040 (2022).
41. G. A. Kwong, S. Ghosh, L. Gamboa, C. Patriotis, S. Srivastava, S. N. Bhatia, Synthetic biomarkers: A twenty-first century path to early cancer detection. *Nat. Rev. Cancer* **21**, 655–668 (2021).
42. E. A. Klein, D. Richards, A. Cohn, M. Tummala, R. Lapham, D. Cosgrove, G. Chung, J. Clement, J. Gao, N. Hunkapiller, A. Jamshidi, K. N. Kurtzman, M. V. Seiden, C. Swanton, M. C. Liu, Clinical validation of a targeted methylation-based multi-cancer early detection test using an independent validation set. *Ann. Oncol.* **32**, 1167–1177 (2021).
43. J. Li, Y. Li, L. Huo, R. Sun, X. Liu, Q. Gu, A. Li, S. Han, H. Liu, Y. Li, Y. Zhang, Detection of serum HE4 levels contributes to the diagnosis of lung cancer. *Oncol. Lett.* **25**, 255 (2023).
44. G. R. Oxnard, T. Maddala, E. Hubbell, A. Aravanis, N. Zhang, O. Venn, A. Valouev, L. Shen, S. Patel, A. Jamshidi, K. Jagadeesh, S. Gross, D. Filippova, J. F. Beausang, M. C. Liu, D. A. Richards, S. Plevritis, R. T. Williams, A.-R. Hartman, C. Swanton, Genome-wide sequencing for early stage lung cancer detection from plasma cell-free DNA (cfDNA): The Circulating Cancer Genome Atlas (CCGA) study. *J. Clin. Oncol.* **36**, LBA8501 (2018).
45. S. Connal, J. M. Cameron, A. Sala, P. M. Brennan, D. S. Palmer, D. J. Palmer, H. Perlow, M. J. Baker, Liquid biopsies: The future of cancer early detection. *J. Transl. Med.* **21**, 118 (2023).
46. N. Liang, B. Li, Z. Jia, C. Wang, P. Wu, T. Zheng, Y. Wang, F. Qiu, Y. Wu, J. Su, J. Xu, F. Xu, H. Chu, S. Fang, X. Yang, C. Wu, Z. Cao, L. Cao, Z. Bing, H. Liu, L. Li, C. Huang, Y. Qin, Y. Cui, H. Han-Zhang, J. Xiang, H. Liu, X. Guo, S. Li, H. Zhao, Z. Zhang, Ultrasensitive detection of circulating tumour DNA via deep methylation sequencing aided by machine learning. *Nat. Biomed. Eng.* **5**, 586–599 (2021).
47. W. Guo, X. Chen, R. Liu, N. Liang, Q. Ma, H. Bao, X. Xu, X. Wu, S. Yang, Y. Shao, F. Tan, Q. Xue, S. Gao, J. He, Sensitive detection of stage I lung adenocarcinoma using plasma cell-free DNA breakpoint motif profiling. *EBioMedicine* **81**, 104131 (2022).
48. X. Zhou, P. Wang, Y. Li, Y. Han, J. Chen, K. Tang, L. Shi, Y. Zhang, R. Zhang, Z. Lin, Accurate DNA sequence prediction for sorting target-chirality carbon nanotubes and manipulating their functionalities. *ACS Nano* **19**, 2665–2676 (2025).
49. Z. Lin, Y. Yang, A. Jagota, M. Zheng, Machine learning-guided systematic search of DNA sequences for sorting carbon nanotubes. *ACS Nano* **16**, 4705–4713 (2022).
50. M. Bennasar, Y. Hicks, R. Setchi, Feature selection using joint mutual information maximisation. *Expert Syst. Appl.* **42**, 8520–8532 (2015).
51. M. B. Kursa, W. R. Rudnicki, Feature selection with the Boruta package. *J. Stat. Softw.* **36**, 1–13 (2010).
52. N. V. Chawla, K. W. Bowyer, L. O. Hall, W. P. Kegelmeyer, SMOTE: Synthetic minority over-sampling technique. *J. Artif. Int. Res.* **16**, 321–357 (2002).
53. H. He, Y. Bai, E. A. Garcia, S. Li, "ADASYN: Adaptive synthetic sampling approach for imbalanced learning" in *2008 IEEE International Joint Conference on Neural Networks* (IEEE World Congress on Computational Intelligence) (IEEE, 2008), pp. 1322–1328.
54. J. Bergstra, R. Bardenet, Y. Bengio, B. Kégl, "Algorithms for hyper-parameter optimization" in *Proceedings of the 25th International Conference on Neural Information Processing Systems* (NIPS'11) (Curran Associates, 2011), pp. 2546–2554.
55. F. Karl, T. Pielok, J. Moosbauer, F. Pfisterer, S. Coors, M. Binder, L. Schneider, J. Thomas, J. Richter, M. Lang, E. C. Garrido-Merchán, J. Branke, B. Bischl, Multi-objective hyperparameter optimization in machine learning—An overview. *ACM Trans. Evol. Learn. Optim.* **3**, 1–50 (2023).
56. H. Chen, I. C. Covert, S. M. Lundberg, S.-I. Lee, Algorithms to estimate Shapley value feature attributions. *Nat. Mach. Intell.* **5**, 590–601 (2023).
57. N. Mantel, The detection of disease clustering and a generalized regression approach. *Cancer Res.* **27**, 209–220 (1967).
58. P. Legendre, M.-J. Fortin, Comparison of the Mantel test and alternative approaches for detecting complex multivariate relationships in the spatial analysis of genetic data. *Mol. Ecol. Resour.* **10**, 831–844 (2010).
59. M. E. Zaslavsky, E. Craig, J. K. Michuda, N. Sehgal, N. Ram-Mohan, J.-Y. Lee, K. D. Nguyen, R. A. Hoh, T. D. Pham, K. Röltgen, B. Lam, E. S. Parsons, S. R. Macwana, W. DeJager, E. M. Drapeau, K. M. Roskin, C. Cunningham-Rundles, M. A. Moody, B. F. Haynes, J. D. Goldman, J. R. Heath, R. S. Chinthrajah, K. C. Nadeau, B. A. Pinsky, C. A. Blish, S. E. Hensley, K. Jensen, E. Meyer, I. Balboni, P. J. Utz, J. T. Merrill, J. M. Guthridge, J. A. James, S. Yang, R. Tibshirani, A. Kundaje, S. D. Boyd, Disease diagnostics using machine learning of B cell and T cell receptor sequences. *Science* **387**, eadp2407 (2025).
60. Q. Du, C. Yan, S. G. Wu, W. Zhang, C. Huang, Y. Yao, L. Wang, Q. Zhang, Q. Liu, J. Guan, Y. Hou, Z. Li, A. Soh, A. Beshiri, Q. Wang, X. Li, Y. Zheng, H. Wang, Development and validation of a novel diagnostic nomogram model based on tumor markers for assessing cancer risk of pulmonary lesions: A multicenter study in Chinese population. *Cancer Lett.* **420**, 236–241 (2018).
61. X. Li, Y. Xu, L. Zhang, Serum CA153 as biomarker for cancer and noncancer diseases. *Prog. Mol. Biol. Transl. Sci.* **162**, 265–276 (2019).
62. Q. Lin, X. Y. Chen, W. F. Liu, P. W. Zhu, W. Q. Shi, B. Li, Q. Yuan, Y. L. Min, J. M. Liu, Y. Shao, Diagnostic value of CA-153 and CYFRA 21-1 in predicting intraocular metastasis in patients with metastatic lung cancer. *Cancer Med.* **9**, 1279–1286 (2020).
63. B. Li, Q. Yuan, Y. T. Zou, T. Su, Q. Lin, Y. Q. Zhang, W. Q. Shi, R. B. Liang, Q. M. Ge, Q. Y. Li, Y. Shao, CA-125, CA-153, and CYFRA21-1 as clinical indicators in male lung cancer with ocular metastasis. *J. Cancer* **11**, 2730–2736 (2020).
64. H. Satoh, H. Ishikawa, K. Kurishima, Y. T. Yamashita, M. Ohtsuka, K. Sekizawa, Cut-off levels of NSE to differentiate SCLC from NSCLC. *Oncol. Rep.* **9**, 581–583 (2002).
65. K. M. Johnston, B. S. Sheffield, S. Yip, P. Lakzadeh, C. Qian, J. Nam, Costs of in-house genomic profiling and implications for economic evaluation: A case example of non-small cell lung cancer (NSCLC). *J. Med. Econ.* **23**, 1123–1129 (2020).
66. R. A. van Amerongen, V. P. Retèl, V. M. Coupé, P. M. Nederlof, M. J. Vogel, W. H. van Harten, Next-generation sequencing in NSCLC and melanoma patients: A cost and budget impact analysis. *Ecancermedicalscience* **10**, 684 (2016).
67. L. M. Sabatini, C. Mathews, D. Ptak, S. Doshi, K. Tynan, M. R. Hegde, T. L. Burke, A. D. Bossler, Genomic sequencing procedure microcosting analysis and health economic cost-impact analysis: A report of the Association for Molecular Pathology. *J. Mol. Diagn.* **18**, 319–328 (2016).
68. S. Kumar, A. Bennett, P. A. Campbell, G. Palidwor, B. Lo, T. J. Perkins, S. Nochaiwong, H. S. Sekhon, D. J. Stewart, K. Thavorn, Costs of next-generation sequencing assays in non-small cell lung cancer: A micro-costing study. *Curr. Oncol.* **29**, 5238–5246 (2022).

Acknowledgments: Z.L. acknowledges supports from the National Key Research and Development Program of China (no. 2023YFA0915200), the National Natural Science Foundation of China (NSFC nos. 52273265 and 52573294), the Guangdong Basic and Applied Basic Research Foundation (no. 2024A1515012437 and 2024B1515040023), the R&D Program of Guangzhou (no. 2025A04J7015), the GJYC program of Guangzhou (no. 2024D03J0002 and 2024D01J0057), the Fundamental Research Funds for the Central Universities (2025ZYGXZR052), State Key Lab of Luminescent Materials and Devices, South China University of Technology (Skllmd-2026-05), and the Xiaomi Foundation. **Author contributions:** Conceptualization: P.C. and Z.L. Methodology: P.C., X. Zheng, and Z.L. Software: P.C. and Z.L. Validation: P.C., X. Zheng, and Z.L. Formal analysis: P.C. and Z.L. Investigation: P.C., Y.L., J. Li, X. Zhou, Y.W., J. Liu, P.W., and Z.L. Resources: P.C., X. Zheng, X.L., R.C., and Z.L. Data curation: P.C., and Z.L. Writing–original draft: P.C., X. Zheng, and Z.L. Writing–review and editing: P.C. and Z.L. Visualization: P.C. and Z.L. Supervision: X. Zheng and Z.L. Project administration: X. Zheng and Z.L. Funding acquisition: Z.L. **Competing interests:** The authors declare that they have no competing interests. **Data, code, and materials availability:** This study did not generate new materials. All data and code needed to evaluate and reproduce the results in the paper are present in the paper and/or the Supplementary Materials. The custom Python codes used for ML and data analyses in this study has been deposited in Zenodo and is publicly available at https://doi.org/10.5281/zenodo.20829152.

Submitted 30 January 2026
Accepted 25 June 2026
Published 29 July 2026
10.1126/sciadv.aef9530

ScienceAdvances

Integrating structurally defined DNA-carbon nanotube sensors with machine learning for cancer detection

Piaoyi Chen, Xin Zheng, Yinong Li, Jian Li, Xuan Zhou, Yawei Wen, Jialong Liu, Pengbo Wang, Xiaohui Li, Runzhe Chen, and Zhiwei Lin

Sci. Adv. **12** (31), eaef9530. DOI: 10.1126/sciadv.aef9530

Science Advances (ISSN 2375-2548) is published by the American Association for the Advancement of Science. 1200 New York Avenue NW, Washington, DC 20005. The title *Science Advances* is a registered trademark of AAAS.